Electronic Supplementary Material (ESI) for Journal of Materials Chemistry A.

Electronic supplementary information

Origin of performance degradation in high-delithiated Li_xCoO_2: insights from direct atomic simulations using global neural network potentials

Pan Zhang,[1,2] Cheng Shang,[2,3] Zhipan Liu,[2,3] Ji-Hui Yang,[1,2*] and Xin-Gao Gong[1,2*]

[1]*Key Laboratory for Computational Physical Sciences (MOE), State Key Laboratory of Surface Physics, Department of Physics, Fudan University, Shanghai 200433, China*

[2]*Shanghai Qizhi Institution, Shanghai 200232, China*

[3]*Key Laboratory for Computational Physical Sciences (MOE), Shanghai Key Laboratory of Molecular Catalysis and Innovative Materials, Department of Chemistry, Fudan University, Shanghai 200433, China*

Email: jhyang04@fudan.edu.cn; xggong@fudan.edu.cn

Table of Contents

S1 Calculation details *3*

S1.1 SSW Global Optimization and Pathway Sampling 3

S1.2 The training of GNNP 3

S1.3 DFT Calculations for Li_xCoO_2 4

S2 Functional test *5*

S2.1 Density of states 5

S2.2 Lattice constant 6

S2.3 Formation energy and intercalation voltage 8

S2.4 The stability of O1-CoO_2 relative to the O3 phase and the average local magnetic moment of transition metals 9

S3 The training of GNNP *11*

S3.1 RMS errors of force, energy, and stress 11

S3.2 Energy-strain curves 11

S4 Structural transition *13*

S4.1 Structural transition of the pairs with the lowest final state energy 13

S4.2 Formation energy and Intercalation voltage profile 14

S4.3 The arrangement of Li ions in $Li_{0.5}CoO_2$ 15

S4.4 The variation trend of the lattice constant with respect to x 16

S4.5 Stacking-sequence changes 17

S4.6 The migration of Co ions 17

S5 Lattice distortion caused by strain *20*

S5.1 Effect of pure compression and tensile strain on the structures of Li_xCoO_2 (x = 1.00, 0.50, 0.33, 0.00) with uniform and non-uniform distribution of Li ions 20

S5.2 Detailed analysis for the effect of compression strain on the electrode materials $Li_{0.33}CoO_2$ with non-uniform distribution of Li ions 23

S5.3 Detailed analysis for the effect of tensile strain on the electrode materials $Li_{0.33}CoO_2$ with non-uniform distribution of Li ions 24

S5.4 Detailed analysis of the drastically changed process at 8% for $Li_{0.33}CoO_2$ with non-uniform distribution of Li ions 25

S5.5 Effect of alternative strains on the structures of Li_xCoO_2 (x = 1.00, 0.50, 0.33, 0.00) with uniform and non-uniform distribution of Li ions 26

S5.6 Detailed analysis for the effect of alternative strains on the electrode materials $Li_{0.33}CoO_2$ with non-uniform distribution of Li ions 29

S5.7 Effect of alternative strains on the structures of $Li_{0.33}CoO_2$ with uniform and non-uniform distribution of Li ions (repeat tests) 31

References *33*

S1 Calculation details

S1.1 SSW Global Optimization and Pathway Sampling

To sample the global potential energy surface (PES) of Li_xCoO_2 at each specified composition, the SSW global optimization approach[1, 2] as implemented in Large-scale Atomic Simulation with neural network Potential (LASP) code[3] was used. SSW-RS[4] method was used to sample the various paths exhaustively between O3-stacking type Li_xCoO_2 and the final state searched (the O3 phase, the H1-3 phase, or the O1 phase), which depends on the delithiation states. The critical reaction pathways are further verified by computing the associated imaginary frequency and extrapolating transition state (TS) structures toward the initial state (IS) and final state (FS). The convergence criteria for all the structures are the maximum atomic force component below 0.01 eV/Å and stress below 0.01 GPa.

S1.2 The training of GNNP

The SSW-NN method[5, 6], which is now incorporated into the LASP code, is used to produce the GNNP. By reducing the difference between NN and DFT values on total energy, force, and stress, the GNNP is trained using a first-principles density functional theory (DFT) data set. The SSW global PES, which includes a large variety of Li_xCoO_2 compositions, is learned iteratively. The training data set of Li_xCoO_2 contains 21769 structures, which represent various chemical environments ranging from clusters, bulks, layers/surfaces, and a wide variety of chemical compositions for Li_xCoO_2 from Li/Co 0:1 to Li/Co 1:1. Clusters of Li and O atoms can also be found in the training data set. To achieve high accuracy for PES, we used a large set of power-type structure descriptors (PTSDs), including 236 descriptors for each element, including 84 2-body, 132 3-body, and 20 4-body descriptors. The network utilized involves three hidden layers (236-144-80-80-1). To normalize the training data sets, min-max scaling is used. Hyperbolic tangent activation functions were used for the hidden layers, and a linear transformation was applied to the output layer of all networks. To match DFT energy, force, and stress, the limited-memory Broyden-Fletcher-Goldfarb-Shanno (L-BFGS) method is used to minimize the loss function.

S1.3 DFT Calculations for Li_xCoO_2

The Vienna Ab initio Simulation Package (VASP)[7, 8] software and the projector augmented wave (PAW)[9, 10] approaches were used to execute all density-functional theory (DFT)[11, 12] computations. The electronic wave functions were represented in a plane-wave basis set with an energy cutoff of 520 eV. For the Brillouin zone integration, we employed Γ-centered k-point meshes with $N_i = [max(1,25|\vec{b}_i|)]$ points in a reciprocal direction, where b_i is the i-th reciprocal lattice vector. For the electron density and structural optimization, the energy, force, and stress threshold were set at 10^{-5}eV, 0.01 eV/Å, and 0.1 GPa, respectively. Two layers of the theory were considered in functional testing. The generalized gradient approximation (GGA) exchange-correlation functional by Perdew, Burke, and Ernzerhof (PBE)[13] and the recently developed strongly constrained and appropriately normed (SCAN) density functional[14] were employed in the exchange-correlation functional. Dispersion corrections were included using Grimme's DFT-D3 method (vdW).[15] Concurrently, in the description of the strongly correlated Co d electrons, a rotationally invariant Hubbard-U term[16] was used. The U value ranges from 1 to 6 with a step size of 1. To summarize, the functional test investigated following functional combinations of PBE, PBE + U, PBE + vdW, PBE + U + vdW, SCAN, SCAN + vdW, SCAN + U, and SCAN + U + vdW. In order to obtain an excellent GNNP, the functional combinations mentioned above are tested carefully (see the Supplementary Information S2 for details). After a detailed functional test, we select SCAN functional to train the GNNP of Li_xCoO_2.

S2 Functional test

In order to obtain an excellent GNNP, the functional combinations mentioned above are tested carefully from the perspectives of electronic structures, lattice constant, the formation energy of $Li_{0.5}CoO_2$ with respect to $LiCoO_2$ and CoO_2, intercalation voltage of the range $0.0 < x < 0.5$ and $0.5 < x < 1.0$, the stability of O1-CoO_2 relative to the O3 phase and the average local magnetic moment of transition metals in Li_xCoO_2 ($x = 1.0$, 0.5, and 0.0 with O3, monoclinic, and O1 phase, respectively).

S2.1 Density of states

Firstly, we need to select a functional combination used in training GNNP that can accurately characterize electrode materials' electrical conductivity in various de-lithiation states concurrently. The electrical conductivity of Li_xCoO_2 changes substantially from semiconductor at x=1.0 to metallic at x=1.0~0.9 when Li ions are removed, and the metallic characteristic is strengthened with the decreasing of lithium concentration, favoring the process of lithium-ions deintercalation or intercalation.[17, 18] As shown in the density of states of $LiCoO_2$ (Fig. S1), $Li_{0.5}CoO_2$ (Fig. S2), and CoO_2 (Fig. S3), only the functional combinations PBE, PBE+U where U=1.0 (denoted as PBE+U1), PBE+U2, PBE+vdW, PBE+vdW+U1, PBE+vdW+U2, SCAN, and SCAN+vdW can adequately characterize the electrical conductivity of electrode materials in various de-lithiation states concurrently. Other functionals can only describe a portion of the conductivity in different de-lithiation states. For example, although SCAN+U1 can correctly predict the semiconductivity of Li_xCoO_2 at $x = 1.0$ and metallicity at $x = 0.0$, it predicts that the system is semiconductor at x=0.5, which is inconsistent with the experimental results. It's worth mentioning that the SCAN functional has the closest experimental value bandgap in all candidates.

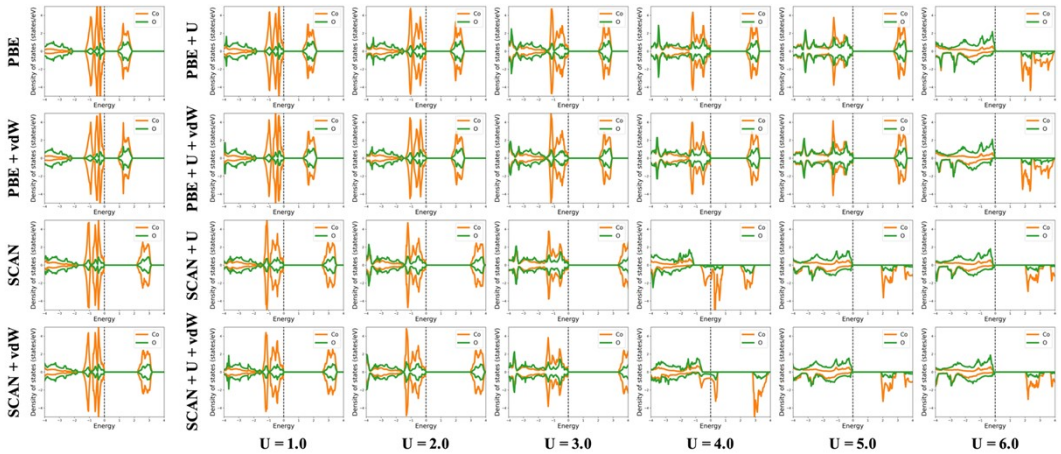

Figure S1. Density of states in states/eV per formula unit for $LiCoO_2$ for the various functionals considered in this study.

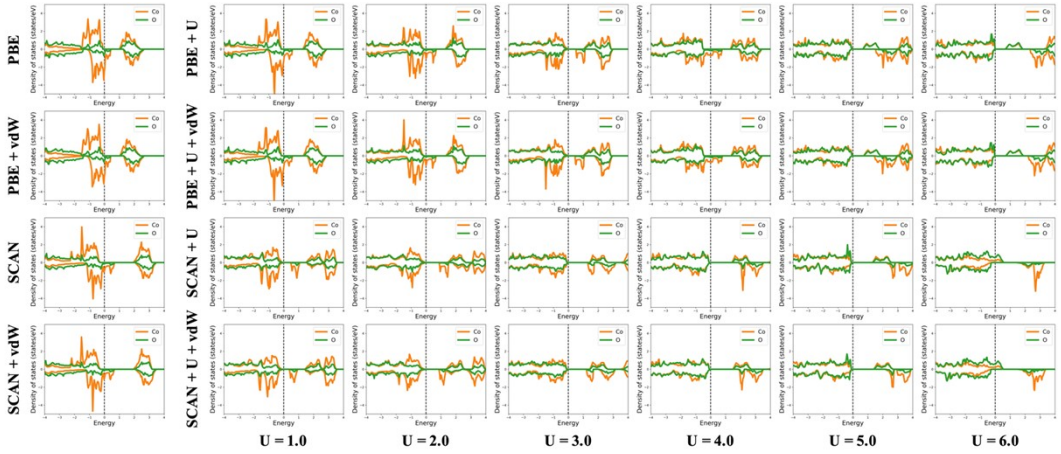

Figure S2. Density of states in states/eV per formula unit for $Li_{0.5}CoO_2$ for the various functionals considered in this study.

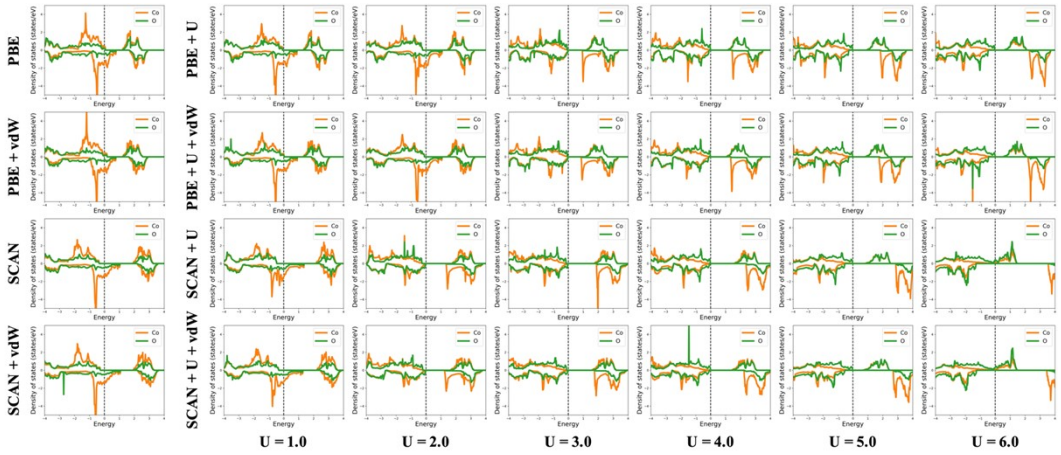

Figure S3. Density of states in states/eV per formula unit for CoO_2 for the various functionals considered in this study.

S2.2 Lattice constant

Secondly, we expect that the functional combination we chose can accurately reflect the lattice constant change trend during the charge and discharge. With the Li ions removed, the lattice constant *c* gradually rises due to the electrostatic repulsion between neighboring O-layers, experiences a maximum at x slightly below 0.5, and progressively decreases. With further extraction of Li ions to limit, the interlayer slab distance decreases rapidly because of the formation of the new stacking types H1-3 and O1. As shown in Fig. S4 (a), although all the functionals we tested can well describe

the changing trend of *c*, the lattice constants are calculated using functionals PBE, PBE+U1, and PBE+U2 deviate significantly from the experimental value 12.879Å[19] at x=0.0. Because the SCAN functional includes medium and short distance interaction, SCAN+vdW will overestimate the system's *c*, resulting in a substantial discrepancy with the experimental measurement.

What's more, lattice variation can also be seen in the lattice constant *a* which undergoes a slight but steady decrease from x=1.0 to x=0.6, followed by a subsequent increase from x=0.4 to x=0.0.[19] As shown in Fig. S4 (b), only PBE+vdW+U2 and SCAN could describe this trend among the remaining functional combinations. In contrast, PBE+vdW shows a continuous downward style inconsistent with the experimental phenomenon. Their comparison with experimental values is listed in Table S1, which shows that SCAN performs better. To select the best functional combination from PBE+vdW+U2 and SCAN, we compared their performance in the formation energy of $Li_{0.5}CoO_2$ with respect to $LiCoO_2$ and CoO_2, intercalation voltage of the range $0.0 < x < 0.5$ and $0.5 < x < 1.0$, the stability of O1-CoO_2 relative to the O3 phase and the average local magnetic moment of transition metals in Li_xCoO_2.

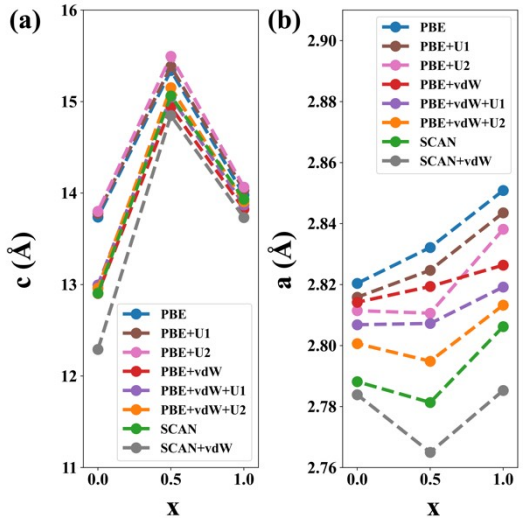

Figure S4. Lattice constant *c* (a) and *a* (b) at different intercalation levels Li_xCoO_2 (x = 0.0, 0.5, and 1.0). The variation trends of lattice constants predicted by PBE+vdW+U2 and SCAN are completely consistent with the experimentally observed results among all functional combinations.

Table S1 Lattice constants of Li_xCoO_2 computed using different functionals and from the experiments. SCAN performs better. For comparison with experimental values, the lattice constant of $Li_{0.5}CoO_2$ along the c-direction is multiplied by 1/3.

	PBE+vdW+U2			SCAN			Expt.			
	a (Å)	*b* (Å)	*c* (Å)	*a* (Å)	*b* (Å)	*c* (Å)	*a* (Å)	*b* (Å)	*c* (Å)	Refs.
$Li_{1.0}CoO_2$	2.813	2.813	13.905	2.806	2.806	13.933	2.817(0)	2.817(0)	14.06(1)	[19]
$Li_{0.5}CoO_2$	4.840	2.795	5.051	4.810	2.781	5.021	4.865(3)	2.809(3)	5.063(3)	[20]

CoO_2	2.801	2.801	12.960	2.788	2.788	12.906	2.8222	2.8222	12.879	[19]

S2.3 Formation energy and intercalation voltage

The formation energy (FE) per formula unit in each de-lithiation state, which shows the relative stability of the structure Li_xCoO_2 against separation into a fraction of x $LiCoO_2$ and a fraction of (1-x) CoO_2, was computed as follows:

$$FE(Li_xCoO_2) = E(Li_xCoO_2) - x \cdot E(LiCoO_2) - (1-x) \cdot E(CoO_2) \#（S1）$$

where x is the fractional amount of Li ions in the system, $E(Li_xCoO_2)$ is the total energy per formula unit in each de-lithiation states, while $E(LiCoO_2)$ and $E(CoO_2)$ represent the total energies per formula unit of the pristine and fully delithiated systems. As shown in Table S2, the formation energy of $Li_{0.5}CoO_2$ estimated using these two functionals is negative, which indicates a solid solution of Li ions in the system, suggesting that Li_xCoO_2 is stable with respect to phase separation into a fraction of 0.5 $LiCoO_2$ and a fraction of 0.5 CoO_2.

The intercalation voltage was estimated using the formula below:[21]

$$V(Li_xCoO_2) = -\frac{E(Li_{x+dx}CoO_2) - E(Li_xCoO_2)}{dx} + E(Li_{bcc}) \#（S2）$$

where $E(Li_{x+dx}CoO_2)$ and $E(Li_xCoO_2)$ represent the total energy per formula unit of the system before and after lithium deintercalation. $E(Li_{bcc})$is the total energy per formula unit of bulk Li. SCAN predicts a higher voltage, but the voltage gap at x = 0.5 estimated using these two functionals, which can also be used as a convenient benchmark for compositional phase stability[22], is almost constant, 0.621 V and 0.643 V for PBE+vdW+U2 and SCAN, respectively. And both voltage profiles of them fall within the range of the voltage curve measured in the experiment (Fig. S5).

Table S2. The FE of $Li_{0.5}CoO_2$ and the intercalation voltage of the range 0.0 < x < 0.5, 0.5 < x < 1.0, and 0.0 < x < 1.0

Functional	FE of $Li_{0.5}CoO_2$ (eV)	Intercalation Voltage (V)		
		0.0<x<0.5	0.5<x<1.0	0.0<x<1.0
PBE+U2+vdW	-0.160	4.511	3.890	4.200
SCAN	-0.155	4.845	4.202	4.524

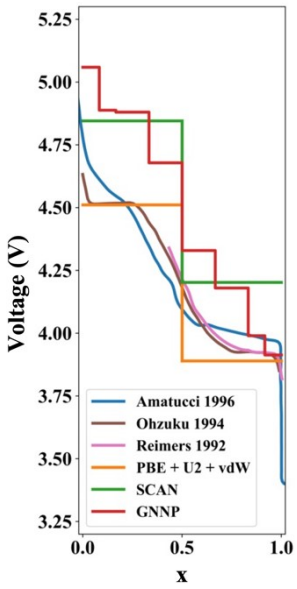

Figure S5. Voltage profiles of Li_xCoO_2 estimated with PBE+U2+vdW, SCAN, and GNNP. Experimental Li_xCoO_2 voltage profiles digitized from previous works[19, 23, 24] summarized by Eric B. Isaacs et.[22].

S2.4 The stability of O1-CoO_2 relative to the O3 phase and the average local magnetic moment of transition metals

As shown in Table S3, both of them can accurately predict that O1-CoO_2 is more stable than O3-CoO_2. In addition, the average local magnetic moments of transition metals under different de-lithiation states estimated using these two functionals are almost identical. While the experimentally measured value at high de-lithiation states are 0.25 μB/Co and 0.15 μB/Co for $Li_{0.5}CoO_2$ and CoO_2, respectively.[25] While the two functionals perform similarly in the above tests, the SCAN functional can predict the bandgap and lattice constant closer to the experimental values.

Table S3. The stability of O1-CoO_2 relative to the O3 phase and the average local magnetic moment of transition metals in Li_xCoO_2.

Functional	Stability of O1-CoO_2 relative to O3 phase (meV / f.u.)			Magnetic moment (μB / atom)		
	E_{O3}	E_{O1}	$E_{O1} - E_{O3}$	x=0.0	x=0.5	x=1.0
PBE+U2+vdW	-18140.267	-18144.415	-4.148	0.998	0.500	0.000
SCAN	-32795.388	-32802.143	-6.755	1.000	0.500	0.000

In conclusion, the results of our tests re-proved that, while no functional tested by us can accurately describe all of the characteristics of Li_xCoO_2 in every de-lithiation state simultaneously, the SCAN functional coincides well with the experimental values in all aspects. This is completely consistent with the results of some recent studies.[22, 26] As a result, we use SCAN to train the GNNP of Li_xCoO_2.

S3 The training of GNNP

S3.1 RMS errors of force, energy, and stress

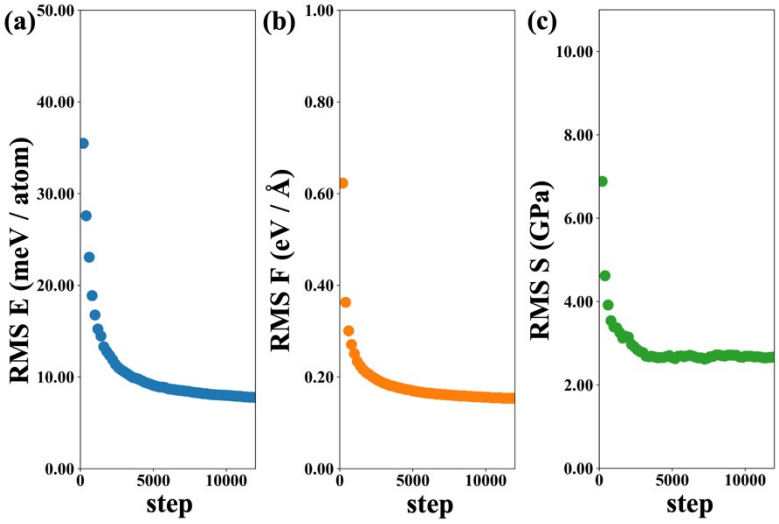

Figure S6. A plot of force, energy, and stress RMS errors on the training sets as a function of the training epoch.

S3.2 Energy-strain curves

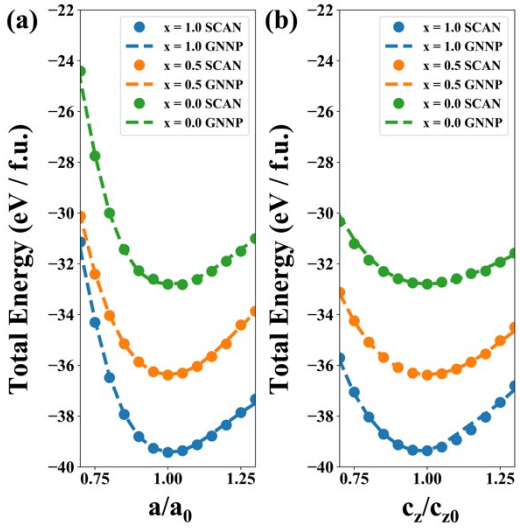

Figure S7. Energy-strain curves for Li_xCoO_2 of different compositions (x = 0.0, 0.5, and 1.0 with O3, monoclinic, and O1 phase, respectively) subjected to single axial

strain along the a-axis (a) and c_z-axis (b). Dashed lines and circle points denote GNNP and SCAN results, respectively. The GNNP model achieves satisfactory accuracy in this test, with the GNNP and SCAN curves virtually overlapping with each other over a large strain range (±30%).

S4 Structural transition

S4.1 Structural transition of the pairs with the lowest final state energy

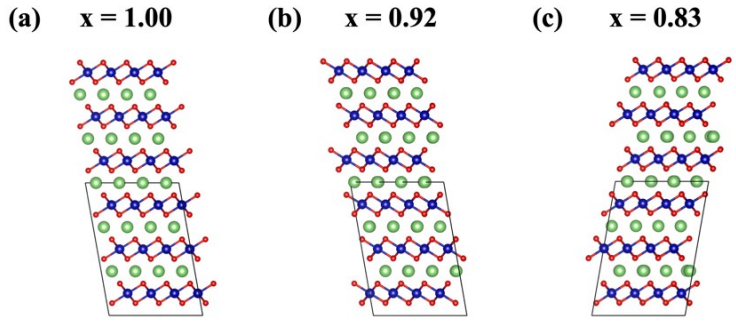

Figure S8. The final state structures with the lowest energy in each de-lithiation state (a) $Li_{1.00}CoO_2$, (b) $Li_{0.92}CoO_2$, (c) $Li_{0.83}CoO_2$. Li ions, Co ions, and O ions are shown in green, blue, and red, respectively. These final state structures are entirely consistent with the experimentally observed results.

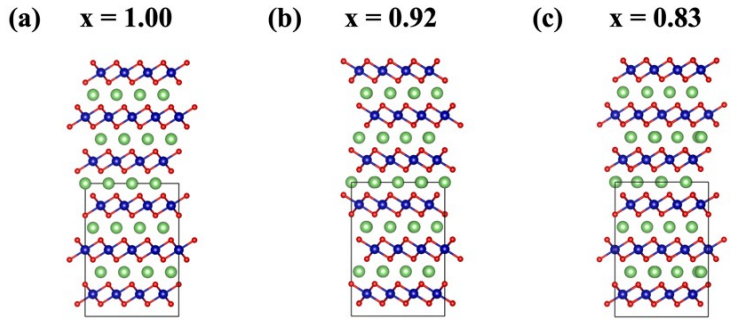

Figure S9. The initial-state structures with the lowest final state energy in each de-lithiation state, (a) $Li_{1.00}CoO_2$, (b) $Li_{0.92}CoO_2$, (c) $Li_{0.83}CoO_2$. Li ions, Co ions, and O ions are shown in green, blue, and red, respectively.

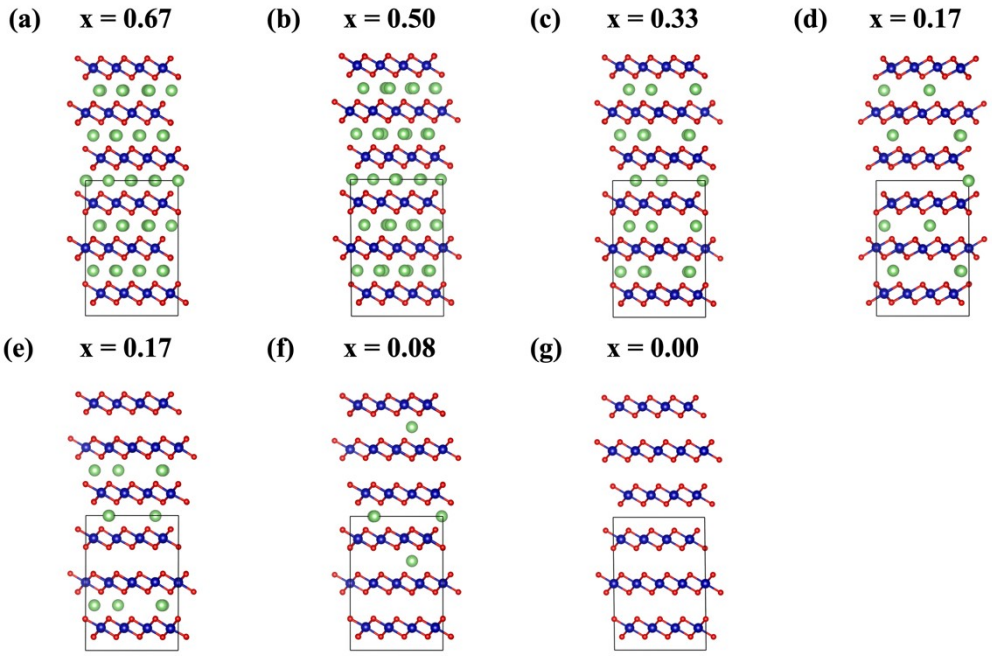

Figure S10. The initial-state structures with the lowest final state energy in each de-lithiation state, (a) $Li_{0.67}CoO_2$, (b) $Li_{0.50}CoO_2$, (c) $Li_{0.33}CoO_2$, (d) $Li_{0.17}CoO_2$, (e) $Li_{0.17}CoO_2$, (f) $Li_{0.08}CoO_2$, and (g) CoO_2. Li ions, Co ions, and O ions are shown in green, blue, and red, respectively.

S4.2 Formation energy and Intercalation voltage profile

The formation energy per formula unit in each de-lithiation state was computed based on the structures with the lowest energy shown in the manuscript to understand the formation of solid solutions of lithiated and de-lithiated Li_xCoO_2 using Eqns. S1. In Fig. S11a, the convex hull is drawn to connect the lowest formation energies in each de-lithiation state. The formation energy of all partially lithiated Li_xCoO_2 is negative, suggesting that Li_xCoO_2 is stable with respect to phase separation into a fraction of x $LiCoO_2$ and a fraction of (1-x) CoO_2. The negative formation energy also indicates a solid solution of Li ions in the system, which is consistent with experiments.[19] For example, the formation energy for half lithiated Li_xCoO_2 (x = 0.5) estimated using GNNP is -172.156 meV/f.u., which is slightly lower than the value -160.731 meV/f.u. calculated by SCAN and the value published by Arup Chakraborty and colleagues using the SCAN functional (0.16 eV/f.u.)[26] because of the formation of a new arrangement of Li ions discussed in the manuscript and Supplementary Information S4.3.

The configurations, which fall on the convex hull of the formation energy, are utilized to construct the theoretical voltage curve using the Eqns. S2. As shown in Fig. S11b, although the calculated result will be higher than the experimental value, the overall change trend is consistent with the voltage curve measured in the experiment.

The result higher than the experimental value is consistent with the SCAN functional test result that the SCAN functional will overestimate the voltage value.

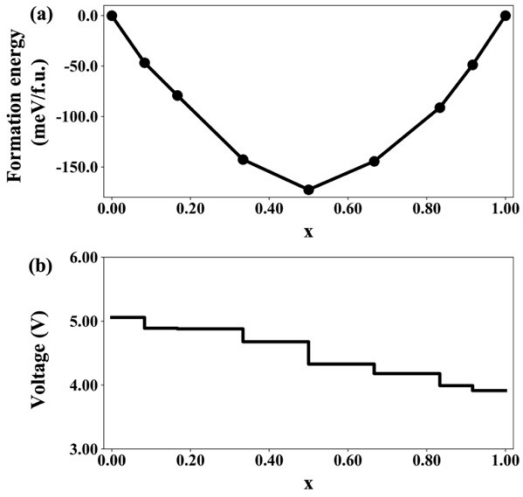

Figure S11. (a) The formation energy per formula unit and (b) Intercalation voltage profile estimated using final state with the lowest energy in each de-lithiation state.

S4.3 The arrangement of Li ions in $Li_{0.5}CoO_2$

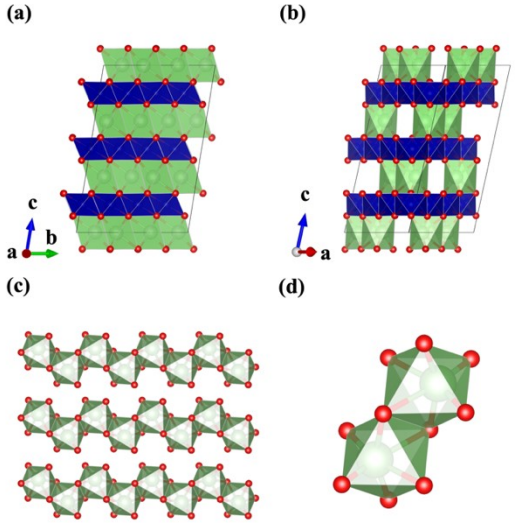

Figure S12. Front view (a) and the side view (b) of the arrangement of Li ions in $Li_{0.5}CoO_2$. (c) The Li ions arrangement of a single layer. (d) More detailed presentation of the adjacent Li ions. Li ions, Co ions, and O ions are shown in green blue, and red, respectively. In order to show the arrangement of Li ions more clearly, we hide Co ions. A zig-zag type of Li ions arrangement can be found in $Li_{0.5}CoO_2$ with the lowest energy in (c) and (d). Li ions will deviate from the center of the oxygen octahedron due to Coulomb interactions between adjacent Li ions.

S4.4 The variation trend of the lattice constant with respect to x

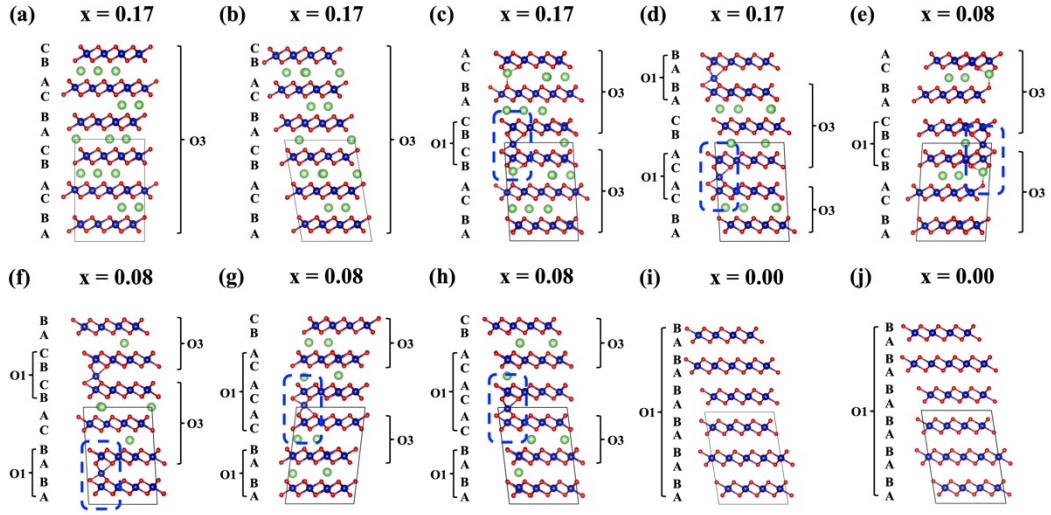

Figure S13. Final state structures with the lowest lattice constants in the high de-lithiation state. (a-d) $Li_{0.17}CoO_2$, (e-h) $Li_{0.08}CoO_2$, (i-j) CoO_2. Blue dotted boxes are used to mark local defects related to Co ions. Li ions, Co ions, and O ions are shown in green, blue, and red, respectively. In the high de-lithiation state, different degrees of H1-3 phase are formed in the system, and the migration of Co ions to the Li ions layer generally occurs.

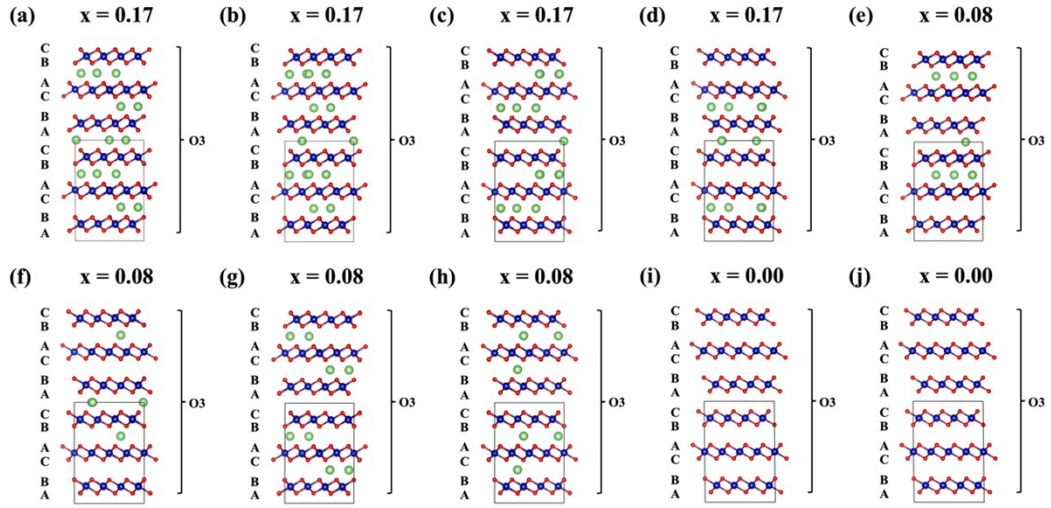

Figure S14. The initial-state structures of the final state with the lowest lattice constants in the high de-lithiation state. (a-d) $Li_{0.17}CoO_2$, (e-h) $Li_{0.08}CoO_2$, (i-j) CoO_2. Li ions, Co ions, and O ions are shown in green, blue, and red, respectively.

S4.5 Stacking-sequence changes

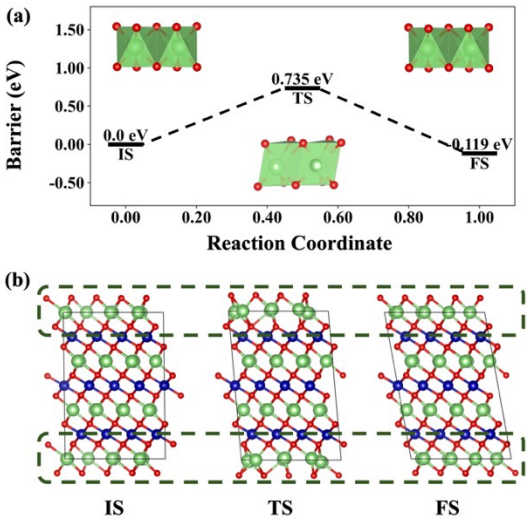

Figure S15. (a) The barrier profile for the stacking-sequence changes of $Li_{0.67}CoO_2$ with the lowest barrier and the nearest gliding distance. The local environment of Li ions is shown in the illustration. (b) The corresponding stacking sequence change pathway. Green dotted boxes are used to mark the local environment of Li ions. Li ions, Co ions, and O ions are shown in green, blue, and red, respectively.

S4.6 The migration of Co ions

Notably, Frenkel-type defect pairs are widely observed at high de-lithiation states. Their formation pathways are further verified by computing the associated imaginary frequency and extrapolating TS structures toward the IS and FS. There are two types of defect formation mechanisms identified with or without the company of the Li ion at the top of Co ions. The structure of $Li_{0.33}CoO_2$ was modified to demonstrate the two mechanisms clearly. In order to eliminate the contribution of the transport of unimportant Li ion to the barrier, the coordinates of the initial and final states of Li ions far from the defect are set at the same coordinates. In addition, the Li ions around the defect, which were affected by the defect formation process, were removed. Therefore, we're discussing these two mechanisms in $Li_{0.31}CoO_2$ and $Li_{0.29}CoO_2$ in the framework of $Li_{0.33}CoO_2$.

In the first defect formation pathway (Fig. S16a-S16e), firstly, there will be the migration of a Li ion to adjacent vacant octahedral sites through a tetrahedral site according to the divacancy mechanism[27] with a barrier of 0.164eV (Fig. S17a). The distance between the Li ion and the Co ion below the tetrahedral site gradually decreases, making the Coulomb interaction between them steadily enhanced. And then, the Co ion inserts into the tetrahedral site through the intervening triangular oxygen face between the tetrahedral site in the Li ions layer and the octahedral sites in the Co

ions layer, where the concentration of Li ions is low, leaving a Co vacancy in the octahedron site in the CoO_2 layer with a barrier of 0.909eV (Fig. S17a). In the second pathway (from Fig. S16f-S16h), the Co ion migrates directly to the tetrahedron in the Li ions layer with a higher barrier of 1.458 eV (Fig. S17b). Therefore, the Li ions transported according to the divacancy mechanism will make the migration of Co ions have a smaller potential barrier. Depending on the Li ion environment surrounding the Co ion, the Co ion in the tetrahedral position may return to its original position again or enter the oxygen octahedron of the Li ion layer forming the crystal nucleus of the spinel phase. Compared with the interior of the bulk, the surface of the electrode materials is more likely to form the spinel phase due to the uneven distribution of Li ions and a higher Li ion flux. What's more, the smaller layer spacing makes the Coulombic interaction between Li and transition metal ions stronger, and the transport of Li ions with the divacancy mechanism would lead to the formation of a vast number of substitution defects during the cycle.

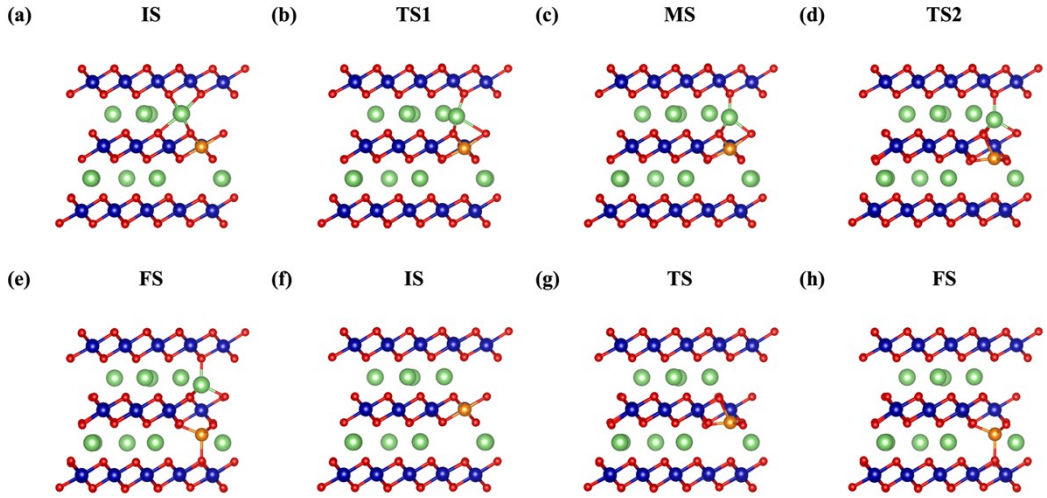

Figure S16. The two migration pathways of Co ions. Figs. (a-e) illustrate the first migration pathway of Co ions. Figs. (f-h) show the second migration pathway of Co ions. Li ions, Co ions, and O ions are shown in green, blue, and red, respectively. In order to mark the migration path of Co ions more clearly, we marked the migrated Co ions as golden.

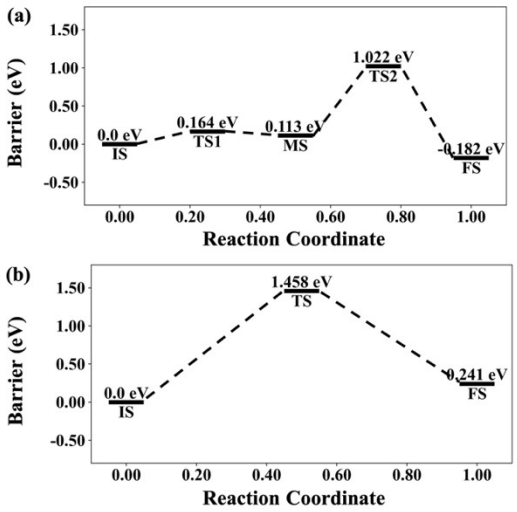

Figure S17. (a) The barrier profile for the first pathway of Co ions. (b) The barrier profile for the second pathway of Co ions. The Li ions transported according to the divacancy mechanism will make the migration of Co ions have a smaller potential barrier.

S5 Lattice distortion caused by strain

S5.1 Effect of pure compression and tensile strain on the structures of Li_xCoO_2 (x = 1.00, 0.50, 0.33, 0.00) with uniform and non-uniform distribution of Li ions

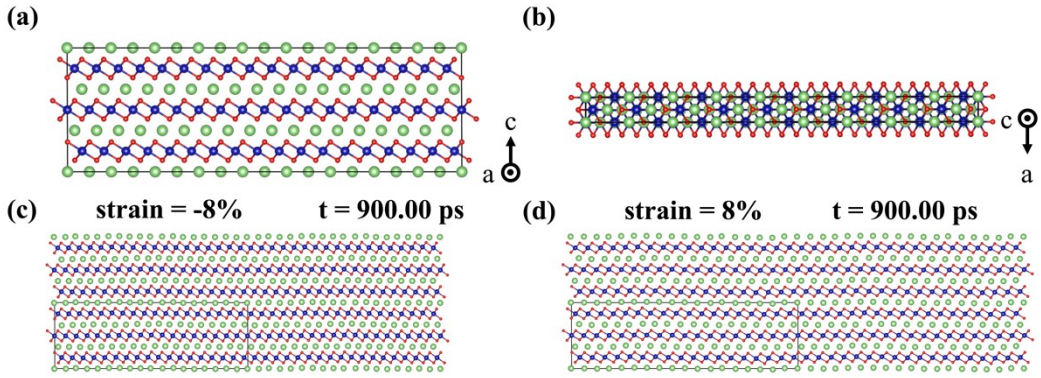

Figure S18. Structures of $LiCoO_2$ under zero, compressive, and tensile strains. (a) Front and (b) top view of initial $LiCoO_2$ supercells under zero strains. (c) Structure of $LiCoO_2$ under a -8% compressive strain after 900 ps MD simulations at 300 K. (d) Structure of $LiCoO_2$ under an 8% tensile strain after 900 ps MD simulations at 300 K. Li, Co, and O are shown in green, blue, and red, respectively. When the compressive and tensile strain is gradually increased, the system does not show any apparent changes except that the Co-O bond lengths are changed to fit the stress caused by the strain.

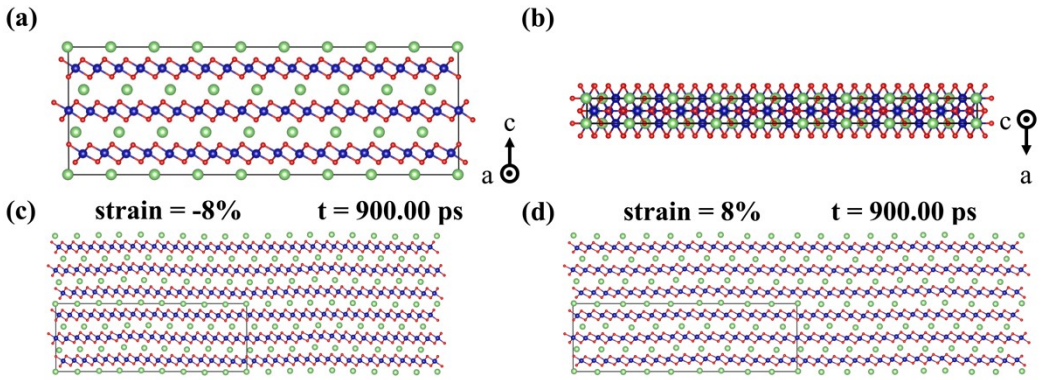

Figure S19. Structures of $Li_{0.50}CoO_2$ with the uniform distribution of Li ions under zero, compressive, and tensile strains. (a) Front and (b) top view of initial $Li_{0.50}CoO_2$ supercells under zero strains. (c) Structure of $Li_{0.50}CoO_2$ under a -8% compressive strain after 900 ps MD simulations at 300 K. (d) Structure of $Li_{0.50}CoO_2$ under an 8% tensile strain after 900 ps MD simulations at 300 K. Li, Co, and O are shown in green,

blue, and red, respectively. When the compressive and tensile strain is gradually increased, the system does not show any apparent changes except that the Co-O bond lengths are changed to fit the stress caused by the strain.

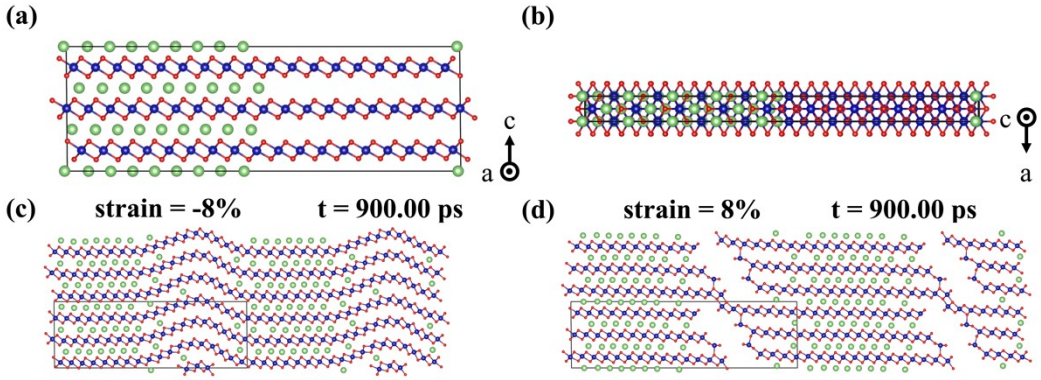

Figure S20. Structures of $Li_{0.50}CoO_2$ with the non-uniform distribution of Li ions under zero, compressive, and tensile strains. (a) Front and (b) top view of initial $Li_{0.50}CoO_2$ supercells under zero strains. (c) Structure of $Li_{0.50}CoO_2$ under a -8% compressive strain after 900 ps MD simulations at 300 K. (d) Structure of $Li_{0.50}CoO_2$ under an 8% tensile strain after 900 ps MD simulations at 300 K. Li, Co, and O are shown in green, blue, and red, respectively. When the compressive strain is applied, curved layers appear in the regions with a relatively sparse Li ion concentration. When the tensile strain is applied, the blockage of the original Li ion migration channels and the formation of new channels can be directly observed due to the fracture of the CoO_2 layers.

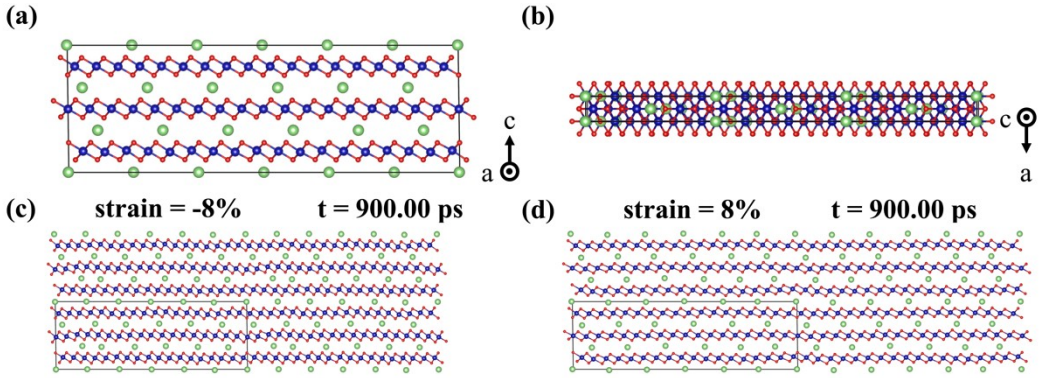

Figure S21. Structures of $Li_{0.33}CoO_2$ with the uniform distribution of Li ions under zero, compressive, and tensile strains. (a) Front and (b) top view of initial $Li_{0.33}CoO_2$ supercells under zero strains. (c) Structure of $Li_{0.33}CoO_2$ under a -8% compressive strain after 900 ps MD simulations at 300 K. (d) Structure of $Li_{0.33}CoO_2$ under an 8% tensile strain after 900 ps MD simulations at 300 K. Li, Co, and O are shown in green, blue, and red, respectively. When the compressive and tensile strain is gradually increased, the system does not show any apparent changes except that the Co-O bond lengths are changed to fit the stress caused by the strain.

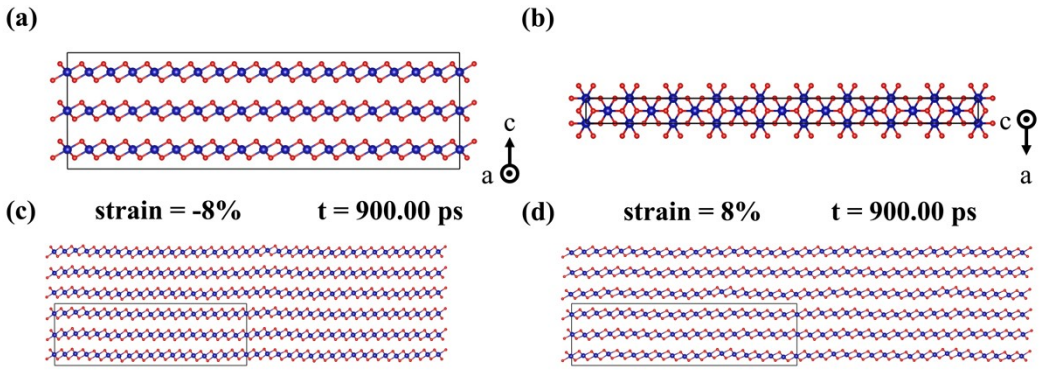

Figure S22. Structures of CoO_2 under zero, compressive, and tensile strains. (a) Front and (b) top view of initial CoO_2 supercells under zero strains. (c) Structure of CoO_2 under a -8% compressive strain after 900 ps MD simulations at 300 K. (d) Structure of CoO_2 under an 8% tensile strain after 900 ps MD simulations at 300 K. Co, and O are shown in blue and red, respectively. When the compressive and tensile strain is gradually increased, the system does not show any apparent changes except that the Co-O bond lengths are changed to fit the stress caused by the strain.

S5.2 Detailed analysis for the effect of compression strain on the electrode materials $Li_{0.33}CoO_2$ with non-uniform distribution of Li ions

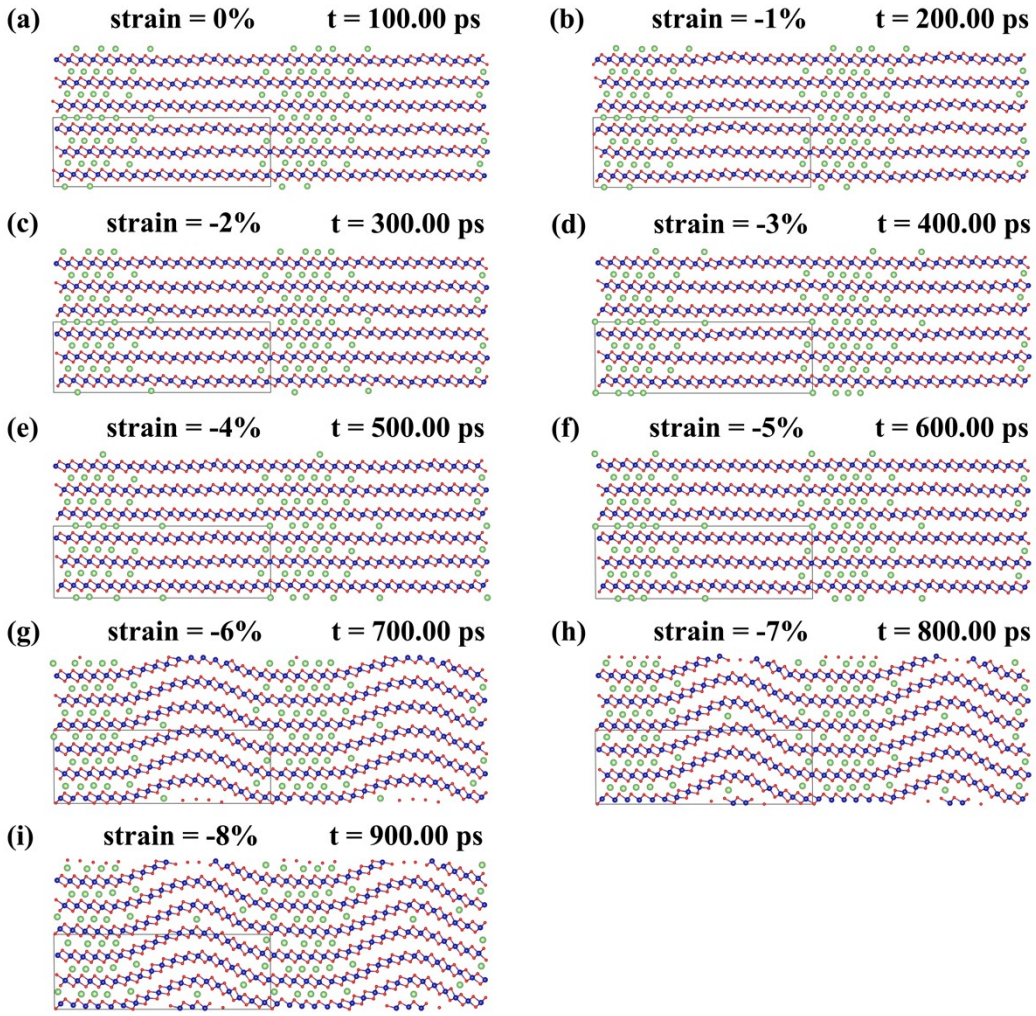

Figure S23. A more detailed evolutionary process for $Li_{0.33}CoO_2$ with non-uniform distribution of Li ions to show the effect of compression strain on the electrode materials. Li ions, Co ions, and O ions are shown in green, blue, and red, respectively. When the compressive strain is applied, curved layers appear in the regions with a relatively sparse Li ion concentration, which has been widely observed experimentally.

S5.3 Detailed analysis for the effect of tensile strain on the electrode materials $Li_{0.33}CoO_2$ with non-uniform distribution of Li ions

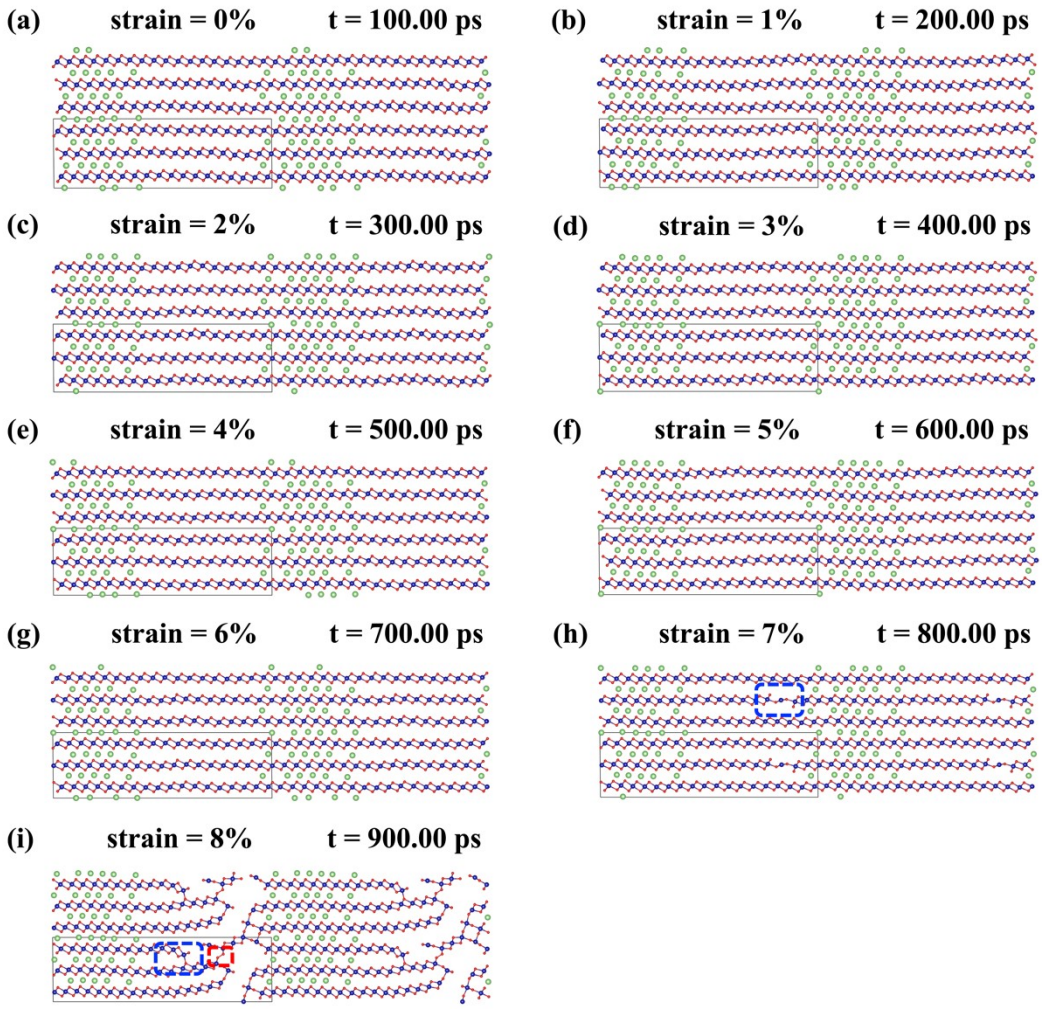

Figure S24. A more detailed evolutionary process for $Li_{0.33}CoO_2$ with non-uniform distribution of Li ions to show the effect of tensile strain on the electrode materials. Blue and red dotted boxes are used to mark local defects related to Co and O ions, respectively. Li ions, Co ions, and O ions are shown in green, blue, and red, respectively. When the tensile strain is applied, the blockage of the Li ion transport channels, the formation of new Li ion transport channels, and the formation of oxygen dimers at crack tips can be observed due to the fracture of the CoO_2 layers.

S5.4 Detailed analysis of the drastically changed process at 8% for $Li_{0.33}CoO_2$ with non-uniform distribution of Li ions

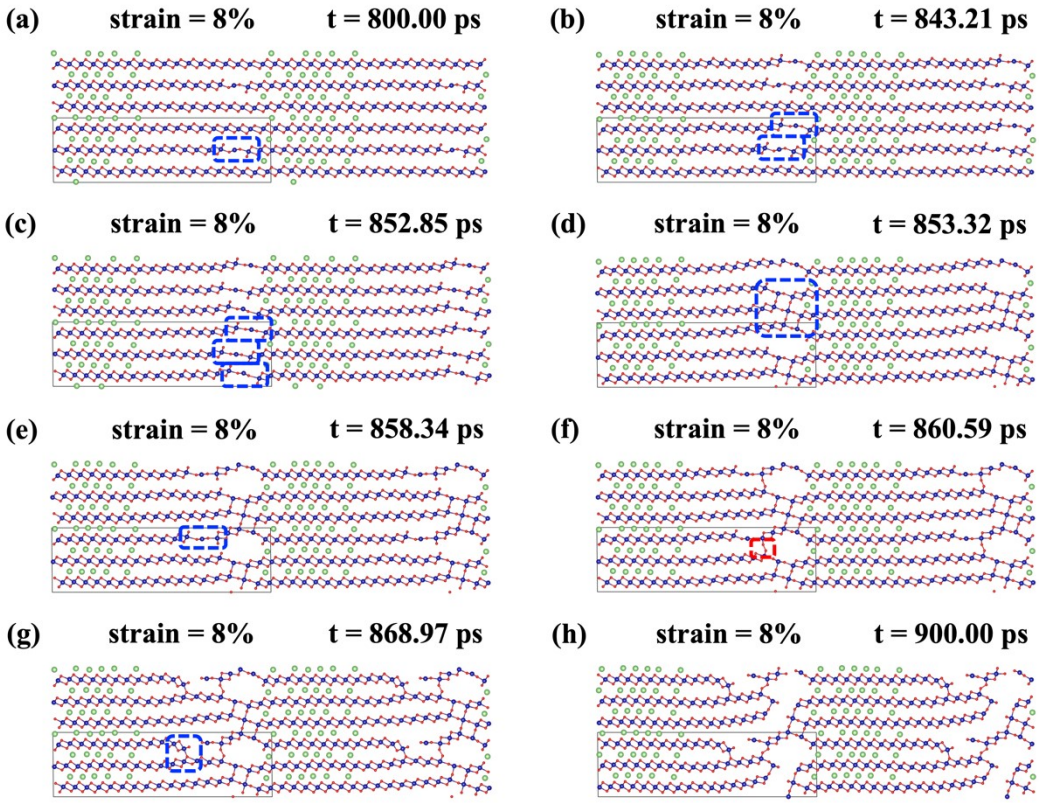

Figure S25. A more detailed evolutionary process for $Li_{0.33}CoO_2$ with non-uniform distribution of Li ions to show the effect of tensile strain at 8% on the electrode materials. Blue and red dotted boxes are used to mark local defects related to Co and O ions, respectively. Li ions, Co ions, and O ions are shown in green, blue, and red, respectively.

S5.5 Effect of alternative strains on the structures of Li_xCoO_2 (x = 1.00, 0.50, 0.33, 0.00) with uniform and non-uniform distribution of Li ions

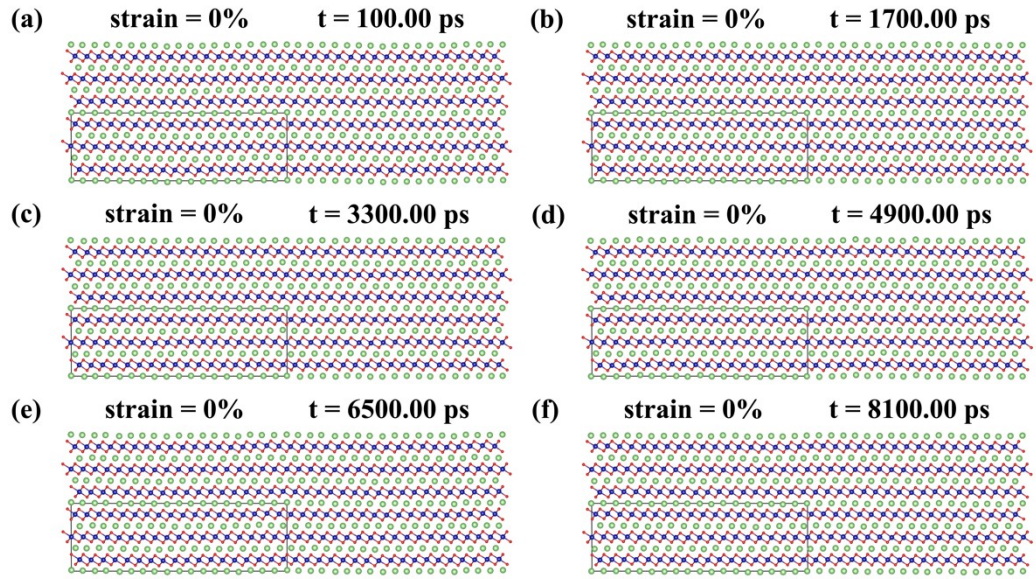

Figure S26. Effect of alternative strains along b-direction on the structures of $LiCoO_2$. (a)-(f) the snapshots when the system is under zero strains. Li ions, Co ions, and O ions are shown in green, blue, and red, respectively. The alternative strains do not cause any damage to the system.

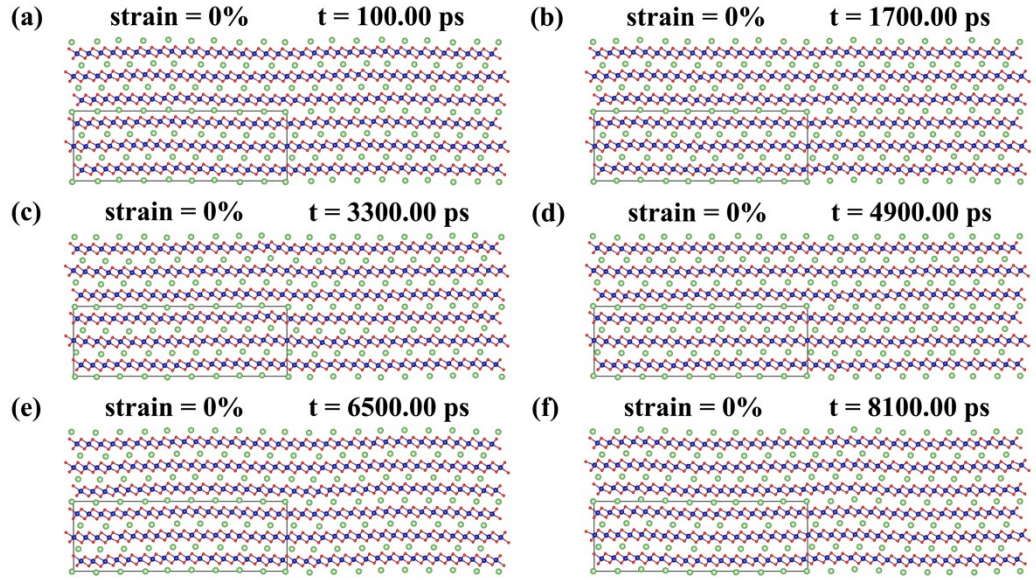

Figure S27. Effect of alternative strains along b-direction on the structures of $Li_{0.50}CoO_2$ with the uniform distribution of Li ions. (a)-(f) the snapshots when the

system is under zero strains. Li ions, Co ions, and O ions are shown in green, blue, and red, respectively. The alternative strains do not cause any damage to the system.

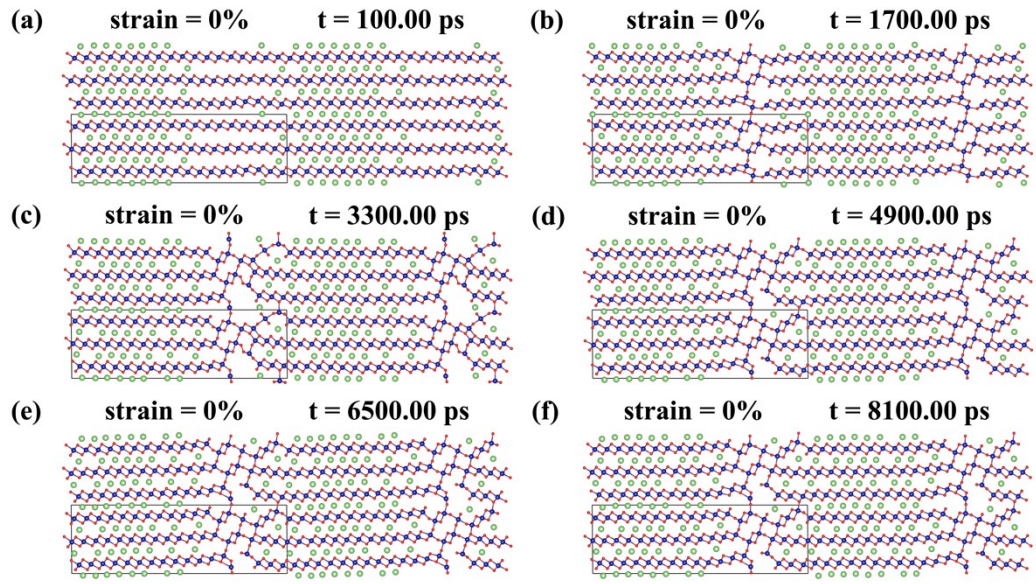

Figure S28. Effect of alternative strains along b-direction on the structures of $Li_{0.50}CoO_2$ with the non-uniform distribution of Li ions. (a)-(f) the snapshots when the system is under zero strains. Li ions, Co ions, and O ions are shown in green, blue, and red, respectively. The alternative strains lead to the blockage of the original Li ion migration channels in the regions with a relatively sparse Li ion concentration due to the fracture of the CoO_2 layers.

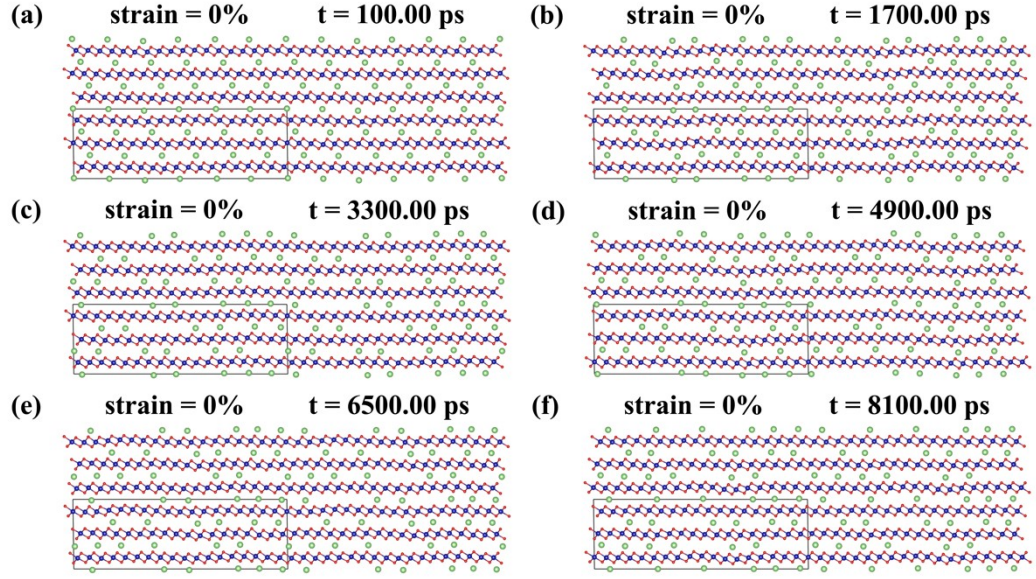

Figure S29. Effect of alternative strains along b-direction on the structures of $Li_{0.33}CoO_2$ with the uniform distribution of Li ions. (a)-(f) the snapshots when the system is under zero strains. Li ions, Co ions, and O ions are shown in green, blue, and red, respectively. The alternative strains do not cause any damage to the system.

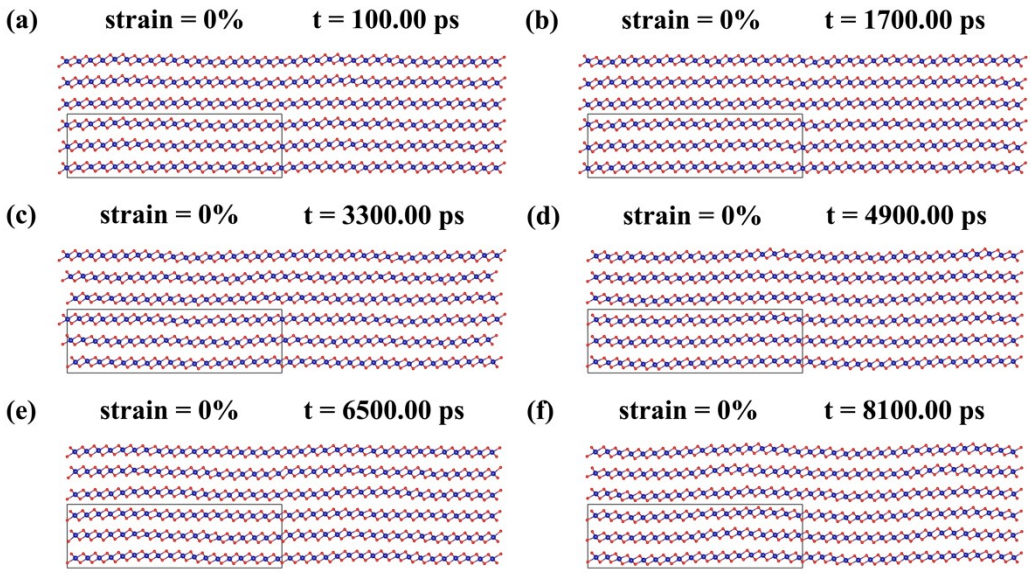

Figure S30. Effect of alternative strains along b-direction on the structures of CoO_2. (a)-(f) the snapshots when the system is under zero strains. Co ions and O ions are shown in blue and red, respectively. The alternative strains do not cause any damage to the system.

S5.6 Detailed analysis for the effect of alternative strains on the electrode materials $Li_{0.33}CoO_2$ with non-uniform distribution of Li ions

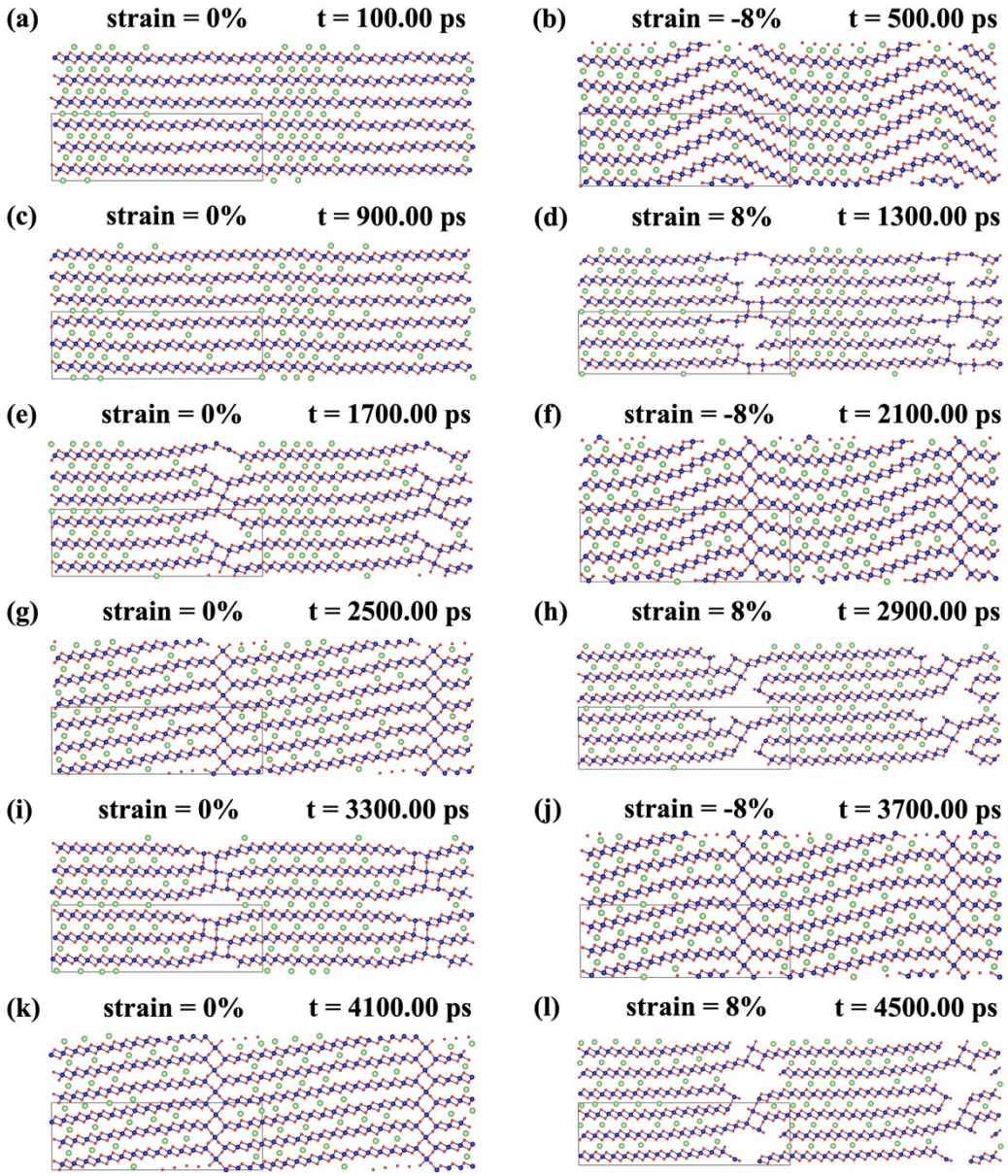

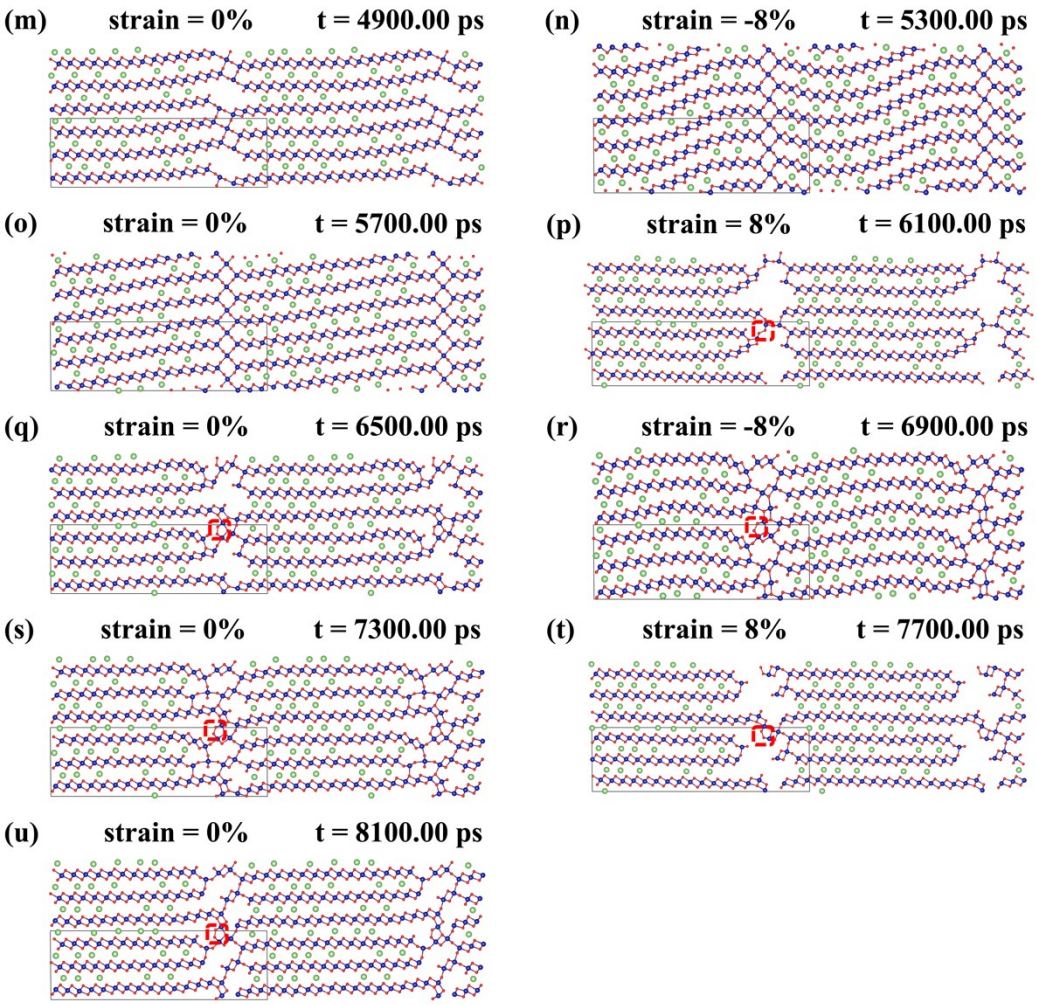

Figure S31. A more detailed evolutionary process to show the effect of alternative strains along b-direction on the structures of $Li_{0.33}CoO_2$ with the non-uniform distribution of Li ions. Blue and red dotted boxes are used to mark local defects related to Co and O ions, respectively. Li ions, Co ions, and O ions are shown in green, blue, and red, respectively.

S5.7 Effect of alternative strains on the structures of $Li_{0.33}CoO_2$ with uniform and non-uniform distribution of Li ions (repeat tests)

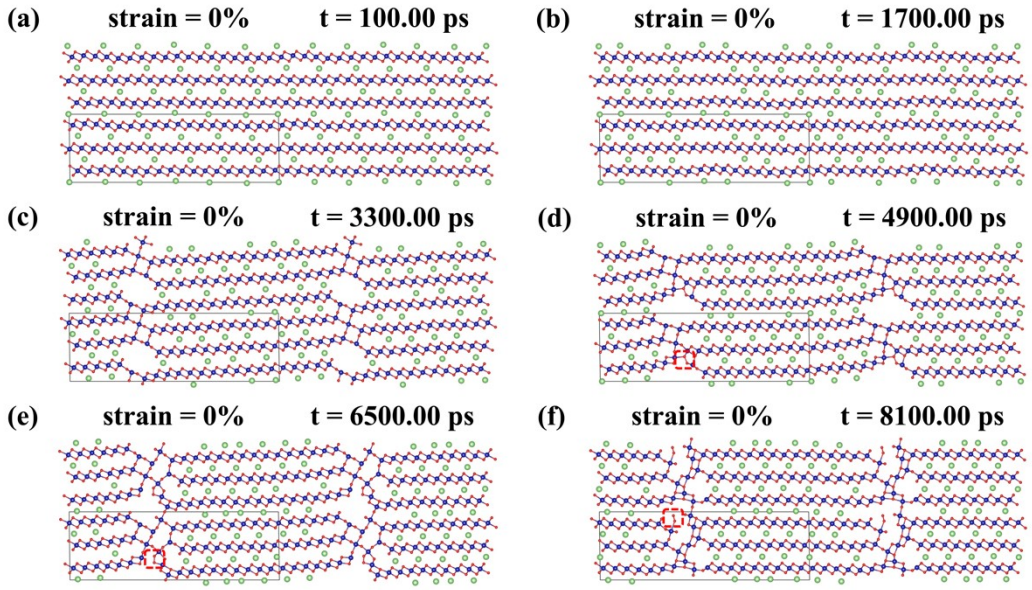

Figure S32. Effect of alternative strains along b-direction on the structures of $Li_{0.33}CoO_2$ with the uniform distribution of Li ions. (a)-(f) the snapshots when the system is under zero strains. Li ions, Co ions, and O ions are shown in green, blue, and red, respectively. The local inhomogeneity caused by the migration of lithium ions leads to the destruction of the system.

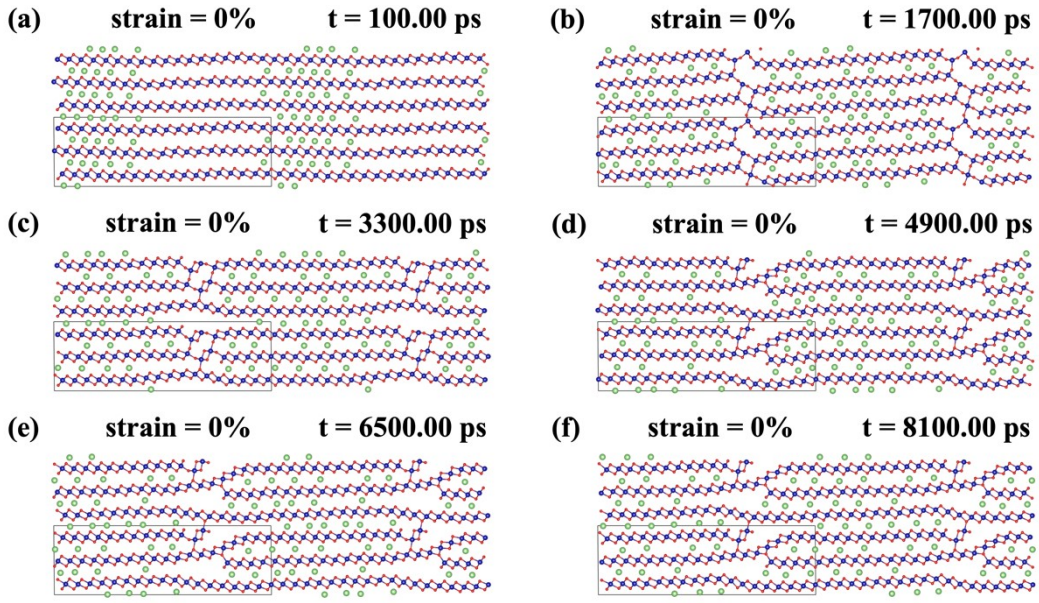

Figure S33. Effect of alternative strains along b-direction on the structures of $Li_{0.33}CoO_2$ with the non-uniform distribution of Li ions. (a)-(f) the snapshots when the system is under zero strains. Li ions, Co ions, and O ions are shown in green, blue, and red, respectively. The local inhomogeneity caused by the migration of lithium ions leads to the destruction of the system. The dislocation structure in the system improves the chemical-mechanical stability of electrode materials.

References

1. C. Shang and Z.-P. Liu, *Journal of Chemical Theory and Computation*, 2013, **9**, 1838-1845.
2. C. Shang, X.-J. Zhang and Z.-P. Liu, *Physical Chemistry Chemical Physics*, 2014, **16**, 17845-17856.
3. S. D. Huang, C. Shang, P. L. Kang, X. J. Zhang and Z. P. Liu, *Wiley Interdisciplinary Reviews: Computational Molecular Science*, 2019, **9**, e1415.
4. X.-J. Zhang and Z.-P. Liu, *Physical Chemistry Chemical Physics*, 2015, **17**, 2757-2769.
5. S.-D. Huang, C. Shang, X.-J. Zhang and Z.-P. Liu, *Chemical science*, 2017, **8**, 6327-6337.
6. S.-D. Huang, C. Shang, P.-L. Kang and Z.-P. Liu, *Chemical science*, 2018, **9**, 8644-8655.
7. G. Kresse and J. Furthmüller, *Physical review B*, 1996, **54**, 11169.
8. G. Kresse and J. Furthmüller, *Computational materials science*, 1996, **6**, 15-50.
9. P. E. Blöchl, *Physical review B*, 1994, **50**, 17953.
10. G. Kresse and D. Joubert, *Physical review b*, 1999, **59**, 1758.
11. P. Hohenberg and W. Kohn, *Physical review*, 1964, **136**, B864.
12. W. Kohn and L. J. Sham, *Physical review*, 1965, **140**, A1133.
13. J. P. Perdew, K. Burke and M. Ernzerhof, *Physical review letters*, 1996, **77**, 3865.
14. J. Sun, A. Ruzsinszky and J. P. Perdew, *Physical review letters*, 2015, **115**, 036402.
15. S. Grimme, J. Antony, S. Ehrlich and H. Krieg, *The Journal of chemical physics*, 2010, **132**, 154104.
16. S. L. Dudarev, G. A. Botton, S. Y. Savrasov, C. Humphreys and A. P. Sutton, *Physical Review B*, 1998, **57**, 1505.
17. J. Van Elp, J. Wieland, H. Eskes, P. Kuiper, G. Sawatzky, F. De Groot and T. Turner, *Physical Review B*, 1991, **44**, 6090.
18. J. Molenda, A. Stokłosa and T. Bąk, *Solid State Ionics*, 1989, **36**, 53-58.
19. G. Amatucci, J. Tarascon and L. Klein, *Journal of The Electrochemical Society*, 1996, **143**, 1114.
20. Y. Takahashi, N. Kijima, K. Tokiwa, T. Watanabe and J. Akimoto, *Journal of Physics: Condensed Matter*, 2007, **19**, 436202.
21. M. Aydinol, A. Kohan, G. Ceder, K. Cho and J. Joannopoulos, *Physical Review B*, 1997, **56**, 1354.
22. E. B. Isaacs, S. Patel and C. Wolverton, *Physical Review Materials*, 2020, **4**, 065405.
23. T. Ohzuku and A. Ueda, *Journal of The Electrochemical Society*, 1994, **141**, 2972.
24. J. N. Reimers and J. Dahn, *Journal of the Electrochemical Society*, 1992, **139**, 2091.

25. T. Motohashi, T. Ono, Y. Sugimoto, Y. Masubuchi, S. Kikkawa, R. Kanno, M. Karppinen and H. Yamauchi, *Physical Review B*, 2009, **80**, 165114.
26. A. Chakraborty, M. Dixit, D. Aurbach and D. T. Major, *npj Computational Materials*, 2018, **4**, 1-9.
27. A. Van der Ven and G. Ceder, *Electrochemical and Solid-State Letters*, 2000, **3**, 301.